

MAMMOTH-LyC: Investigating the Role of Galaxy Mergers in a Strong Lyman Continuum Leaker at $z = 2.39$

SHENGZHE WANG,^{1,2} XIN WANG,^{2,1,3} MATTHEW A. MALKAN,⁴ HARRY I. TEPLITZ,⁵ REBECCA L. DAVIES,⁶ KARL GLAZEBROOK,⁶ KEUNHO J. KIM,⁵ THEMIS Y NANAYAKKARA,⁶ HANG ZHOU,² YIMING YANG,^{1,2} CHAO-WEI TSAI,^{1,3,2} YUXUAN PANG,² ZHENG CAI,⁷ XIAOHUI FAN,⁸ ALAINA HENRY,⁹ ZIHAO LI,^{10,11} DONG DONG SHI,¹² XIAN ZHONG ZHENG,¹³ AND ZHIYU YAN¹

¹*National Astronomical Observatories, Chinese Academy of Sciences, Beijing 100101, China*

²*School of Astronomy and Space Science, University of Chinese Academy of Sciences (UCAS), Beijing 100049, China*

³*Institute for Frontiers in Astronomy and Astrophysics, Beijing Normal University, Beijing 102206, China*

⁴*Department of Physics and Astronomy, University of California, Los Angeles, 430 Portola Plaza, Los Angeles, CA 90095, USA*

⁵*Infrared Processing and Analysis Center, Caltech, 1200 E. California Blvd., Pasadena, CA 91125, USA*

⁶*Centre for Astrophysics and Supercomputing, Swinburne University of Technology, Hawthorn, VIC 3122, Australia*

⁷*Department of Astronomy, Tsinghua University, Beijing 100084, China*

⁸*Steward Observatory, University of Arizona, 933 North Cherry Ave., Tucson, AZ 85721, USA*

⁹*Space Telescope Science Institute, 3700 San Martin Drive, Baltimore, MD 21218, USA*

¹⁰*Cosmic Dawn Center (DAWN), Denmark*

¹¹*Niels Bohr Institute, University of Copenhagen, Jagtvej 128, DK2200 Copenhagen N, Denmark*

¹²*Center for Fundamental Physics, School of Mechanics & Optoelectronic Physics, Anhui University of Science and Technology, Huainan 232001, China*

¹³*Tsung-Dao Lee Institute and State Key Laboratory of Dark Matter Physics, Shanghai Jiao Tong University, Shanghai 201210, China*

ABSTRACT

The MAMMOTH-LyC survey is a cycle 30 Hubble Space Telescope (HST) medium program obtaining 18-orbit-deep WFC3/UVIS F225W imaging in two massive galaxy protocluster fields at $z \sim 2.2$. We introduce this survey by reporting the discovery of J1244-LyC1, a strong Lyman continuum (LyC) leaker at $z = 2.39$, exhibiting clear merger signatures. J1244-LyC1 has a highly significant (10σ) LyC detection, corresponding to an absolute escape fraction of $f_{\text{esc}} = 36\% \pm 4\%$ (1σ). The LyC emission is spatially resolved into multiple peaks that coincide with the system's disturbed morphology, confirming genuine multi-site LyC leakage. With a stellar mass of $10^{10.2} M_{\odot}$, J1244-LyC1 is both the first confirmed high-redshift LyC-leaking merger and the most massive LyC emitter known to date. We interpret J1244-LyC1 as a merger-driven starburst system in which tidal interactions have disrupted the interstellar medium, creating multiple low-column-density pathways that facilitate LyC escape. This discovery provides the first direct evidence of spatially resolved LyC escape in a merging system, offering new insight into the potential role of major mergers in driving the cosmic reionization.

Keywords: Reionization—Galaxies: Galaxy evolution—galaxies: High-redshift galaxies

1. INTRODUCTION

Lyman continuum (LyC) photons ($\lambda_{\text{rest}} < 912 \text{ \AA}$) produced by galaxies powered the last major cosmic phase transition—the Epoch of Reionization (EoR, $z \sim 6$ –11; Stark 2016), during which the neutral intergalactic medium (IGM) became reionized (Dayal et al. 2020).

Corresponding author: Xin Wang
xwang@ucas.ac.cn

However, the fraction of ionizing photons that successfully escape their host galaxies, f_{esc} , remains one of the most crucial unknowns in understanding the EoR. Constraining this parameter directly addresses a central and long-standing question: what sources reionized the Universe? (Finkelstein et al. 2019; Naidu et al. 2020).

Directly observing LyC-leaking galaxies is essential for answering this question, yet such efforts face a fundamental challenge: the rapidly declining IGM transmission for LyC photons at $z > 4$ (Inoue et al. 2014), which renders direct detections infeasible at the red-

shifts most relevant to reionization. As a result, observational searches for LyC emission have focused on two lower-redshift windows: systems at $z \sim 0.3$ accessible with the Cosmic Origins Spectrograph (COS) on the Hubble Space Telescope (HST) (e.g., Izotov et al. 2016a; Wang et al. 2021), and galaxies at $z \sim 2\text{--}4$ —the “cosmic noon” epoch—using HST/WFC3-UVIS imaging (e.g., Oesch et al. 2018; Marques-Chaves et al. 2024; Wang et al. 2025; Beckett et al. 2025).

At the low-redshift window ($z \sim 0.3$), HST/COS has enabled the construction of a sizable sample of confirmed LyC leakers (Flury et al. 2022; Izotov et al. 2016a; Reste et al. 2025a). These samples have revealed correlations between f_{esc} and several observable diagnostics, including the UV continuum slope β (Chisholm et al. 2022), the Ly α emission-line profile (Flury et al. 2022; Naidu et al. 2022), and the [O III]/[O II] ratio (O32) (Pellegrini et al. 2012). Collectively, these trends indicate that LyC-leaking systems tend to exhibit high specific star-formation rates, highly ionized gas, compact star-forming regions, and low H I covering fractions along the lines of sight to their ionizing sources (Jaskot 2025). Several physical mechanisms have been proposed to explain the leakage of ionizing radiation, including suppressed feedback (Jaskot et al. 2017), ionizing feedback (Gazagnes et al. 2018; Flury et al. 2022; Flury et al. 2025; Bait et al. 2024), stellar and supernova-driven feedback (Chisholm et al. 2017; Amorín et al. 2024; Komarova et al. 2021; Flury et al. 2025; Carr et al. 2025), and bursty star formation (Trebetsch et al. 2017; Flury et al. 2025). Yet the physical mechanism that triggers such extreme star-formation episodes remains uncertain.

Galaxy mergers have long been proposed as a mechanism capable of enhancing LyC escape by reshaping the gas morphology and star-formation activity (Bridge et al. 2010; Purkayastha et al. 2022; Reste et al. 2023; Yuan et al. 2024; Zhu et al. 2024). Gas-rich interactions frequently trigger repeated starbursts after pericentric passages (Faria et al. 2025), and merging systems tend to exhibit significantly elevated star-formation rates (SFRs) relative to isolated galaxies, especially during the late stages of interaction (Patton et al. 2013; Stiwerwalt et al. 2015; Ferreira et al. 2024). These intense starbursts efficiently produce large populations of massive stars—thereby increasing the intrinsic LyC photon budget—and can facilitate LyC escape through stellar and supernova-driven feedback (Trebetsch et al. 2017; Barrow et al. 2020; Ma et al. 2020; Choustikov et al. 2024). In addition, tidal forces can redistribute gas away from galactic centers (Pearson et al. 2016), potentially boosting f_{esc} along lines of sight that pass outside the tidally displaced material (Reste et al. 2023; Ejdetjärn

et al. 2025). Cosmological simulations at $z \sim 5\text{--}10$ likewise find that mergers can enhance LyC leakage under simplified f_{esc} prescriptions (Kostyuk & Ciardi 2024). Observationally, in the low- z regime, the Ly α and Continuum Origins Survey (LaCOS) has compiled a sample of 42 LyC leakers, confirming that more than 41% reside in merging systems and establishing mergers as an important channel for LyC escape (Reste et al. 2025b).

In contrast, within the high-redshift window ($z \sim 2\text{--}4$), although many LyC candidates show clear morphological signatures of galaxy interactions, spatial offsets between LyC-band emission and the UV continuum have made it extremely difficult to rule out contamination from low- z interlopers (Zhu et al. 2024). For example, Ion3 (Meštrić et al. 2025; Vanzella et al. 2018) exhibits strong ground-based spectroscopic features yet is dominated by a foreground interloper; its true LyC detection significance is only 3.5σ . Other candidates such as z19863 and CDFS-6664 (Gupta et al. 2024; Yuan et al. 2024) show similar spatial offsets. The intrinsically weak UV continuum associated with these LyC-leaking regions further complicates interpretation and forces a re-evaluation of the physical origin of the claimed LyC signals. In principle, unambiguous confirmation requires high spatial-resolution spectroscopy. Consequently, no high-redshift merger system has yet been securely demonstrated to exhibit significantly enhanced f_{esc} .

In this Letter, we report the discovery of a new LyC emitter at $z = 2.39$ in the BOSS1244 field. This source benefits from extensive multi-band imaging and spectroscopy from both HST and Keck, enabling a detailed investigation of its physical properties. The structure of this paper is as follows: Section 2 describes the observations and data reduction; Section 3 presents our analysis, including spectral-line modeling, spectral energy distribution (SED) fitting, and the calculation of f_{esc} ; and Section 4 discusses the implications of our results. Throughout this work, we adopt a flat Λ CDM cosmology with $H_0 = 70 \text{ km s}^{-1} \text{ Mpc}^{-1}$, $\Omega_M = 0.3$, and $\Omega_\Lambda = 0.7$.

2. OBSERVATIONS

The primary dataset for J1244-LyC1 is drawn from the MAMMOTH (MAppling the Most Massive Overdensity Through Hydrogen) program series (Cai et al. 2016, 2017; Wang et al. 2022; Zhou et al. 2025; Yang et al. 2025; Golden-Marx et al. 2025). These programs target the BOSS1244 protocluster at $z = 2.24 \pm 0.02$, one of the most massive known overdensities at cosmic noon (Cai et al. 2016, 2017). The HST Cycle-28 medium program, the MAMMOTH-Grism survey (GO-

16276; P.I.: X. Wang; [Wang et al. 2022](#)), provided spectroscopic identification across the overdensity, detecting key rest-frame optical lines such as [O III], [O II], H β , and H γ .

In addition, the HST Cycle-30 medium program MAMMOTH-LyC (GO-17159; P.I.: X. Wang) obtained 18 orbits of ultra-deep LyC-band (F225W) imaging—probing LyC emission at $z > 2.2$ —over the BOSS1244 field (Fig. 1). The HST observations are complemented by extensive ground-based multi-band data, including CFHT K_s band, LBT U and z band imaging, and Keck/MOSFIRE K band spectroscopy covering H α ([Zhou et al. 2025](#)).

2.1. HST Data and Reduction

High-resolution HST imaging of J1244-LyC1 was obtained with WFC3/UVIS and WFC3/IR from several programs (GO-17159 and GO-16276, P.I.: X. Wang; [Wang et al. 2022](#); GO-15266, P.I.: Z. Cai; [Liu et al. 2023](#)). J1244-LyC1 was observed in F225W, F475W, F125W, and F160W, with total exposure times of $\sim 48,600$ s, ~ 2800 s, ~ 1800 s, and ~ 2600 s, respectively. These probe rest-frame LyC (600–800 Å), UV (1400 Å), and optical (3700–4750 Å) emission. Slitless spectroscopy from the MAMMOTH-Grism survey provides WFC3/G141 grism data ($R \sim 100$), covering [O II], H β , and H γ for J1244-LyC1 ([Wang et al. 2022](#)).

We used the pipeline-calibrated FLC single exposures from MAST as the starting point for UVIS reduction. Cosmic rays were identified and masked using `astroscrappy`. To correct amplifier-dependent background variations, we equalized the background levels across the four readout amplifiers.

Multiple exposures were aligned using an iterative astrometric refinement procedure. The F475W mosaic was first registered to the F160W reference frame from the MAMMOTH-Grism survey, and the F225W exposures were subsequently aligned to the F475W frame. Final mosaics were produced using `AstroDrizzle` v3.7.1 from `DrizzlePac` ([Fruchter & Hook 2002](#)), following the configuration described in [Carter et al. \(2025\)](#). Our input parameters for `Astrodrizzle` are listed in Appendix A. The pixel size of the final F225W and F475W mosaics is 0.03''.

The most significant challenge arose from aligning the ultra-deep 18-orbit F225W imaging. The UV field contains few suitable stars for astrometric solutions, and roughly 30% of the exposures are affected by cosmic-ray contamination, due to full orbit long exposures. In addition, increased pointing uncertainties due to aging HST gyroscopes further complicated the alignment.

To address these issues, we developed a customized reduction framework incorporating affine transformations, iterative drizzling, cosmic-ray rejection, refined photometric matching, and density-based clustering. This procedure achieved a final relative astrometric precision of ~ 0.2 pixel, i.e., ~ 6 milli-arcsec. A detailed description of the method will be presented in the forthcoming data release and initial science results (Wang et al., in preparation).

2.2. Keck Observations

J1244-LyC1 was observed twice using Keck/MOSFIRE: 2022A_U016 (P.I.: M. Malkan; [Zhou et al. 2025](#)) and 2025A_W335 (P.I.: R. Davies). The first observation was obtained on 15 April 2022 in Multi-Object Spectroscopy (MOS) mode, with a 0.7'' slit width and a total exposure time of 7920 s ($11 \times 4 \times 180$ s) under $\sim 0.7''$ seeing. The second observation, carried out on 21 February 2025 in Long-Slit Spectroscopy (LSS) mode, used a 1.0'' slit width and accumulated 3960 s (22×180 s) under $\sim 0.6''$ seeing. The first observation only covered part of the source, the second observation was at a different PA that allowed it to cover both main components.

The reduction procedure follows [Zhou et al. \(2025\)](#). MOSFIRE data were processed with the PYPEIT pipeline ([Prochaska et al. 2020](#)), which performs wavelength calibration using atmospheric OH emission lines. One-dimensional spectra from individual exposures were extracted and co-added to increase the signal-to-noise ratio (SNR). Additional details of our reduction steps are provided in Appendix B.

2.3. Ground-based Imaging

Ground-based imaging includes LBT/LBC U and z band observations and CFHT/WIRCam K_s band data, with total exposure times of 4.7 hr, 4 hr, and 5 hr, respectively. The observations were taken under seeing conditions of 0.8''–1''. These ground-based photometric measurements provide essential constraints for the global SED fitting of J1244-LyC1.

3. ANALYSIS

3.1. LyC Detection

Fig. 1 presents the high-spatial-resolution HST imaging of J1244-LyC1 in F225W, F475W, F125W, and F160W. We adopt the F160W image as the reference and use its 3σ segmentation map to define the aperture. Within this region, the PSF-matched LyC-band measurement reveals a 10σ detection (with $m_{\text{F225W}} = 27.81^{+0.11}_{-0.10}$ AB mag; Table 1).

The LyC emission displays an extended structure whose centroid does not coincide with either of the two

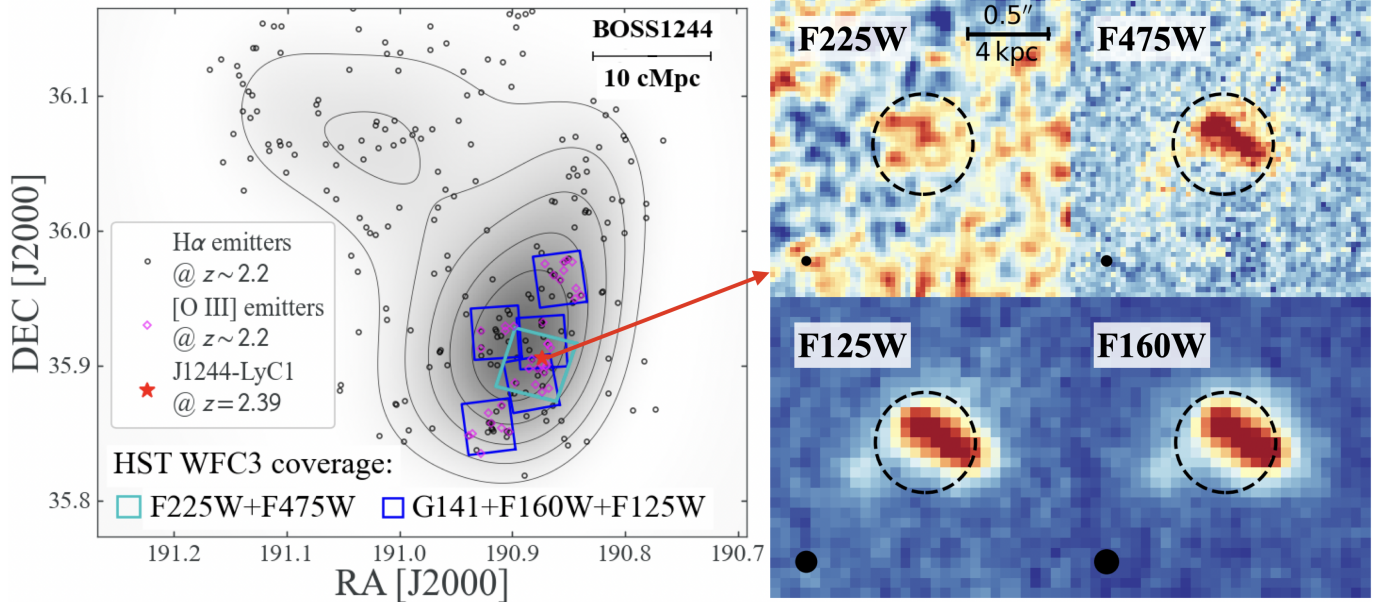


Figure 1. HST WFC3 coverage of the BOSS1244 protocluster field and high-resolution multi-band imaging of J1244-LyC1. LEFT: The MAMMOTH-Grism and MAMMOTH-LyC programs target overdense fields of extreme emission-line galaxies (EELGs) at $z \approx 2.2$, corresponding to the BOSS1244 protocluster. Black circles mark spectroscopically confirmed H α emitters (HAEs; Shi et al. 2021), while the magenta diamonds indicate EELGs with $\text{EW}(\text{[O III]}) > 225 \text{ \AA}$ following Tang et al. (2019), identified using the MAMMOTH-Grism deep HST grism spectroscopy. The red star denotes the location of J1244-LyC1. RIGHT: HST imaging of J1244-LyC1 in WFC3/UVIS F225W (rest-frame LyC; PSF-smoothed), F475W (rest-frame UV), and WFC3/IR F125W and F160W (rest-frame optical). The FWHM of the PSF is shown by the black circle. The 0.6'' aperture is indicated by the black dashed circle. Each cutout is 1.8'' \times 1.8'' in size.

UV luminosity peaks. We further analyze this behavior in Section 4.2, where the system is decomposed into three principal LyC-leaking regions. Although the apparent offset between LyC emission and UV peaks resembles that seen in z19863 and CDFS-6664 (Gupta et al. 2024; Yuan et al. 2024), the dominant LyC-emitting region in J1244-LyC1 lies near the central interface of the merging system, distinct from previously reported cases.

3.2. Spectrum Analysis

3.2.1. Emission Lines

J1244-LyC1 is covered by both *HST* WFC3/G141 grism data ($R \sim 100$) and two Keck/MOSFIRE K band observations ($R = 3600$; Appendix C). The spectra detect [O II], H γ , H β , and H α , with no additional strong emission features. These lines confirm a redshift of $z = 2.39$, and no evidence is found for a low- z interloper.

A portion of the [O III] $\lambda 4959$ line is marginally detected at the edge of the G141 grism coverage. However, because the throughput declines sharply at the bandpass edge and the flux calibration is unreliable, we do not attempt to estimate [O III] fluxes.

Slit-loss corrections were applied to both MOSFIRE datasets by convolving the F160W image with the seeing

of each night and comparing the resulting flux distribution. The median seeing was 0.7'' for the first observation and 0.6'' for the second.

Emission-line fluxes were then measured from the G141 grism and MOSFIRE spectra (see Table 1). No significant [N II], [S II] or [Ne III] detections are found in the spectra.

3.2.2. H α Kinematics

The two Keck observations provide a clear separation of the double velocity components in the H α emission. As shown in Fig 2, the first observation primarily samples one of the two photometric centers and is dominated by the redshifted H α component. The second observation exhibits a substantial shift in the emission peak relative to the first spectrum.

We fitted the H α line in the first observation with a single Gaussian initially, then used its centroid and FWHM as constraints for one of the components in a double-Gaussian model for the second spectrum. This yields a relative velocity difference of $116 \pm 3.6 \text{ km s}^{-1}$ between the two components.

Because the first MOSFIRE observation is seeing-limited and only partially covers the system, we can-

Table 1. Emission line and photometry of J1244-LyC1

H α	H β	[O II]	HST F225W	LBT <i>U</i>	HST F475W	LBT <i>Z</i>	HST F125W	HST F160W	CFHT <i>Ks</i>
8.4 \pm 0.4	2.6 \pm 0.6	5.6 \pm 0.7	27.81 $^{+0.11}_{-0.10}$	25.15 $^{+0.10}_{-0.09}$	24.27 $^{+0.01}_{-0.01}$	24.14 $^{+0.09}_{-0.08}$	23.57 $^{+0.01}_{-0.01}$	23.26 $^{+0.01}_{-0.01}$	22.80 $^{+0.18}_{-0.17}$

NOTE— Observed line fluxes are measured from the WFC3/G141 grism data and Keck MOSFIRE spectra. The unit of line fluxes and multi-band photometry is 10^{-17} erg s $^{-1}$ cm $^{-2}$ and AB mag. All reported uncertainties represent 1σ errors.

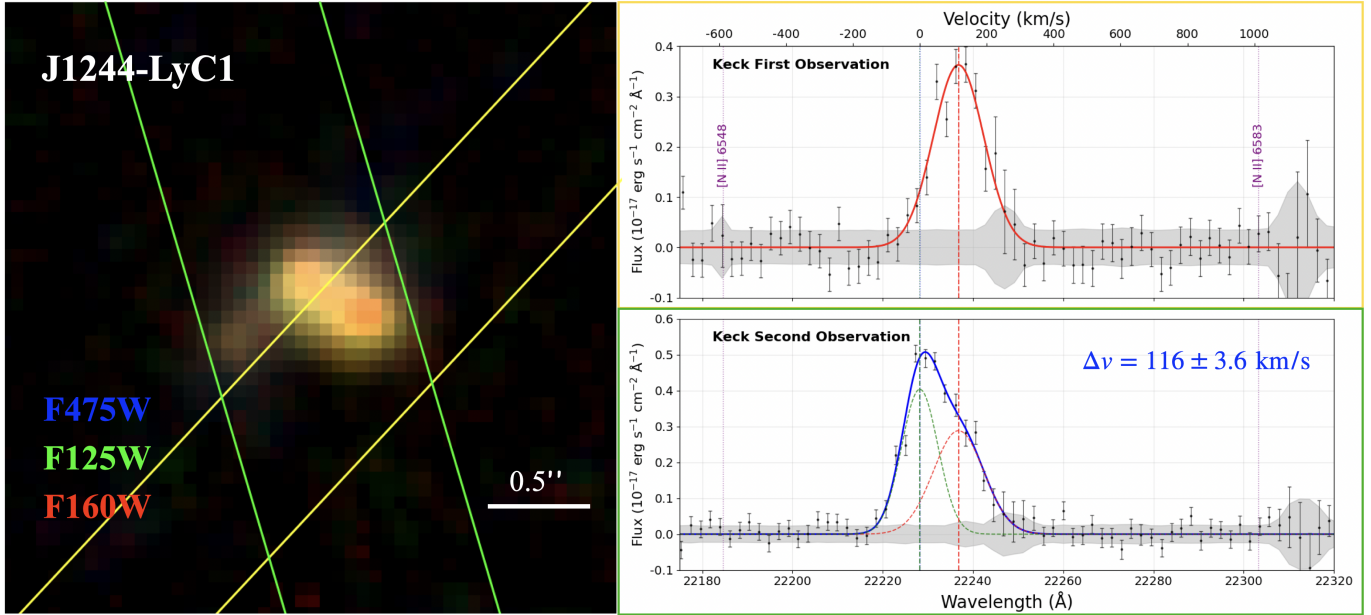


Figure 2. Keck/MOSFIRE *K* band spectroscopy ($R \sim 3600$) confirming the double-velocity components of J1244-LyC1 through the H α emission line. LEFT: Slit positions from two MOSFIRE observations overlaid on the pseudo-color image of J1244-LyC1. The yellow and green rectangles correspond to the slit orientations for the first and second observations, respectively, and match the colors used for the spectra on the right. RIGHT: H α emission-line profiles and Gaussian fitting results. For the first observation, a single-Gaussian model is adopted, and the derived line centroid is used to constrain the double-Gaussian fit in the second observation. Because the blue component is closer to the systemic redshift of J1244-LyC1 ($z = 2.387$), we adopt its centroid as the velocity zero-point to illustrate the relative velocity offset between the two components. The expected locations of the [N II] $\lambda\lambda 6548, 6583$ lines are marked; no significant [N II] emission is detected in either observation.

not reliably quantify the flux contribution from the second component in that exposure. Thus, the adopted H α fluxes for the blue and red components come exclusively from the second observation: $F_{\text{H}\alpha, \text{red}} = (4.1 \pm 0.32) \times 10^{-17}$ erg s $^{-1}$ cm $^{-2}$, $F_{\text{H}\alpha, \text{blue}} = (4.1 \pm 0.25) \times 10^{-17}$ erg s $^{-1}$ cm $^{-2}$.

3.2.3. Dust Extinction

Given detections of both H α and H β , we estimated the nebular reddening using the Balmer decrement under a Milky Way extinction curve:

$$E(B - V) = \frac{2.5}{k_{\text{H}\beta} - k_{\text{H}\alpha}} \log_{10} \left(\frac{(\text{H}\alpha/\text{H}\beta)}{R_0} \right), \quad (1)$$

where $R_0 = 2.86$ for Case B recombination at $T_e = 10^4$ K and $n_e = 10^2$ cm $^{-3}$ (Osterbrock & Ferland 2006). Here,

$k_{\text{H}\alpha}$ and $k_{\text{H}\beta}$ denote the values of the adopted Milky Way reddening curve evaluated at the wavelengths of H α and H β , respectively.

This yields $E(B - V) = 0.15^{+0.27}_{-0.22}$. Because H β is detected only at 4.3σ , the spectroscopic reddening remains uncertain, and we instead adopt the more precise SED-based estimate of $E(B - V) = 0.21 \pm 0.01$ (Section 3.3).

3.2.4. Metallicity

Although [O II] is the only strong metal line detected, we estimate a lower limit on the gas-phase metallicity using the [O II]/H β relation from Sanders et al. (2025):

$$\log \left(\frac{[\text{O II}]}{\text{H}\beta} \right) = 0.172 + 0.954 \cdot x - 0.832 \cdot x^2, \quad (2)$$

where $x = 12 + \log(\text{O/H}) - 8$, and $\log([\text{O II}]/H\beta) = 0.43^{+0.12}_{-0.10}$.

The $[\text{O II}]/H\beta$ relation is calibrated and valid only over $12 + \log(\text{O/H}) \in [7.3, 8.6]$, corresponding to $\log([\text{O II}]/H\beta) \lesssim 0.5$. Since our measured ratio exceeds this threshold at the 1σ upper bound, the relation cannot provide a reliable metallicity upper limit. We therefore adopt the 1σ lower bound of the measured ratio, which corresponds to $12 + \log(\text{O/H}) > 8.19$, as a conservative lower limit for constraining the SED-fitting parameter space. The final SED-fitting results are fully consistent with this metallicity lower limit derived from the emission line fluxes (see Table 2)

Furthermore, while our previous work has examined the resolved metallicity map in this MAMMOTH field (Li et al. 2022) for galaxies with securely detected $[\text{O III}]$ emission lines, the absence of a robust $[\text{O III}]$ line map for this target prevents a reliable estimate of its metallicity map using joint strong-line constraints (i.e., $[\text{O III}]$ and $[\text{O II}]$). Due to the low SNR for each $[\text{O II}]$ and $H\beta$ spaxel, we did not manage to calculate a metallicity map.

3.2.5. Star Formation

With the adopted extinction correction, the dust-corrected $\text{H}\alpha$ luminosity implies $\text{SFR}(\text{H}\alpha) \approx 48 \pm 2.3 M_\odot \text{ yr}^{-1}$ using the Kennicutt (1998) calibration. This value agrees with the SED-derived SFR (Table 2). Given its stellar mass of $\sim 10^{10.2} M_\odot$, the SFR is slightly above that of typical main-sequence galaxies at comparable redshift (Speagle et al. 2014).

The spatial distribution of the SFR on different timescales in J1244-LyC1 is an important quantity for our analysis. The WFC3/G141 grism data provide spatially resolved maps of both $[\text{O II}]$ (Fig. 5) and $H\beta$. However, the $H\beta$ map has insufficient SNR, preventing a reliable SFR map derived directly from Balmer emission. Constructing an SFR map from the $[\text{O II}]$ emission would require a resolved metallicity map (Kewley et al. 2004), but as discussed in Section 3.2.4, the current data do not support a robust spatially resolved metallicity estimate.

Although we cannot derive a full SFR map, the spatial distribution of $[\text{O II}]$ nevertheless traces recent star formation on $\sim 3\text{--}10$ Myr timescales (Kennicutt & Evans 2012). We examine its connection to LyC escape in Section 4.2.

3.3. SED Model Fits

We performed SED fitting to constrain the physical properties of J1244-LyC1, which provides the necessary stellar population information for estimating f_{esc} . The fitting was carried out using the latest version of CIGALE

(v2025; Boquien et al. 2019), and the resulting best-fit SED is shown in Fig. 3. We adopted the Bruzual & Charlot (2003) stellar population synthesis (BC03) model, a delayed exponentially declining star formation history, and the Charlot & Fall (2000) dust attenuation law. The escape fraction f_{esc} was included as a free parameter. The absorption in the U band caused by the blended Lyman-series lines is $\sim 12\%$, as estimated using the IGM model adopted in CIGALE (Meiksin 2006).

The photometric measurements used in the SED fitting include the LBT U and Z bands, the CFHT Ks band, and the HST/WFC3 F336W (LyC), F475W, F125W, and F160W bands. All HST images were PSF-matched to the F160W image to ensure consistent photometry. For the ground-based data, we used the F160W image as a high-resolution prior and employed TPHOT to obtain accurate flux measurements (Yang et al. 2025). The results are summarized in Table 1.

As discussed in Section 3.2, we derived a lower limit on metallicity as well as estimates of $E(B-V)$ and $\text{SFR}_{\text{H}\alpha}$. These spectroscopic measurements were incorporated as constraints in the SED fitting. The derived physical parameters are listed in Table 2.

3.4. Decomposing Images Using GALFIT

Across all available imaging bands, J1244-LyC1 exhibits two bright components and pronounced tidal features (Fig. 1). To characterize its structural properties, we performed two-dimensional surface brightness modeling using GALFIT.

As illustrated in Fig. 3.4, we modeled the F160W image, which provides the highest spatial resolution at a wavelength closest to the Keck/MOSFIRE K band used for the $\text{H}\alpha$ observations. This allows a direct comparison between the morphological substructures and the two kinematic components revealed in the $\text{H}\alpha$ emission.

We carried out both single-Sérsic and double-Sérsic fits. The single-component model leaves substantial residuals, whereas the double-component model provides a significantly improved description of the global morphology. The residual maps further highlight extended tidal structures.

The two components, labeled C1 and C2, have a flux ratio of roughly 1:1.8 and are separated by 2.5 kpc ($0.3''$). Only one component falls within the slit during the first Keck pointing. Combined with the dual $\text{H}\alpha$ velocity components (Section 3.2), which exhibit a relative velocity offset of $116 \pm 3.6 \text{ km s}^{-1}$, these results confirm that J1244-LyC1 is a late-stage major merger.

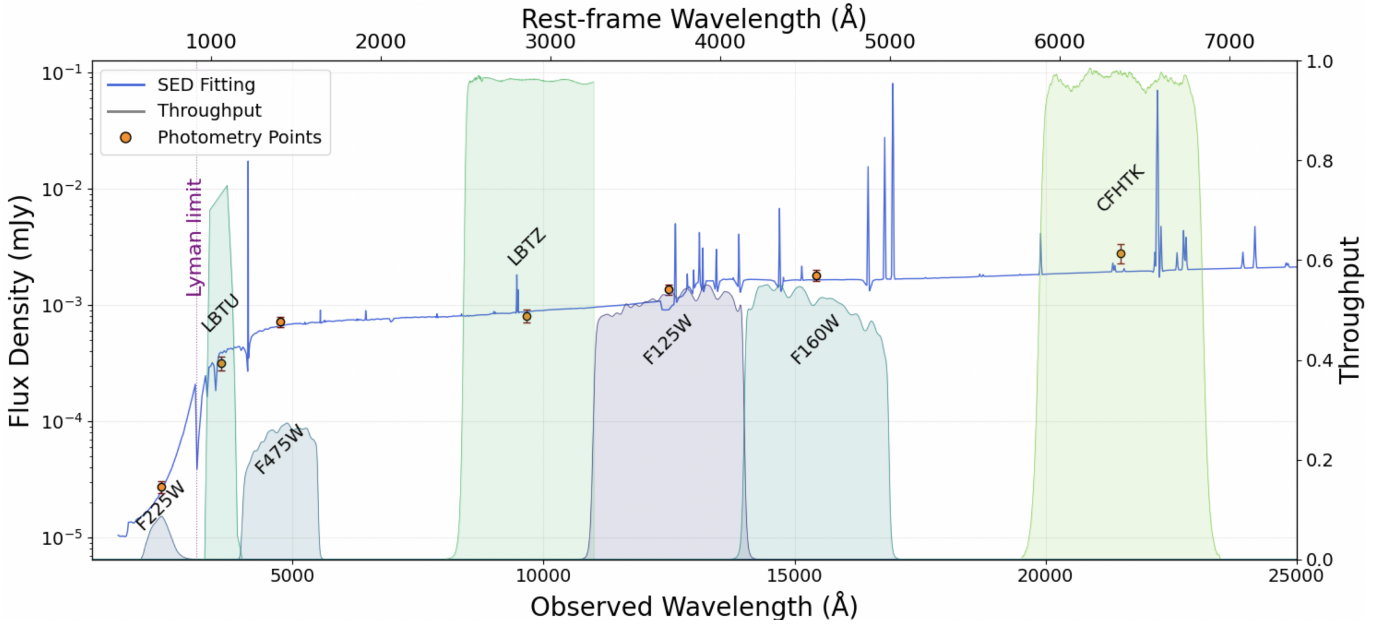


Figure 3. The best-fit SED model (blue) of J1244-LyC1 at $z = 2.39$ using CIGALE, fit to the existing broad-band photometry covering a wide wavelength range of 600–7000 Å in the rest-frame. The SED fitting results are shown in Table 2, and the multi-band photometry is shown in Table 1. The SED of J1244-LyC1 is dominated by a young stellar population with an age 330 ± 120 Myr and a recent SFR of $65 \pm 33 M_{\odot} \text{ yr}^{-1}$.

Table 2. Physical properties of J1244-LyC1 derived from SED fitting

RA	DEC	z_{spec}	$\log(M_{*}/M_{\odot})$	$\text{SFR}_{\text{H}\alpha} (M_{\odot} \text{ yr}^{-1})$	$\text{SFR}_{\text{SED}} (M_{\odot} \text{ yr}^{-1})$	$E(B-V)_{\text{gas}}$	$12 + \log(\text{O/H})$	f_{esc}
190.87348	35.90626	2.387	$10.15_{-0.35}^{+0.19}$	48 ± 2	65 ± 33	0.21 ± 0.01	$8.47_{-0.14}^{+0.11}$	0.37 ± 0.08

NOTE— All reported uncertainties represent 1σ errors.

3.5. LyC Escape Fraction

The escape fraction f_{esc} is constrained observationally by comparing the observed LyC flux to the intrinsic LyC flux expected from stellar population models. Several methods have been developed (Jaskot 2025): (1) using the $\text{H}\beta$ line to quantify nebular absorption of LyC photons (e.g., Izotov et al. 2016; Flury et al. 2022); (2) fitting the multi-band SED while allowing f_{esc} to vary as a free parameter (e.g., Izotov et al. 2016b; Fletcher et al. 2019); and (3) determining the relative escape fraction based on the ratio of ionizing to non-ionizing fluxes, which can be corrected for dust attenuation to obtain the absolute escape fraction (e.g., Steidel et al. 2001; Wang et al. 2025; Gupta et al. 2024; Steidel et al. 2018).

Although J1244-LyC1 shows an $\text{H}\beta$ detection in the HST/WFC3 G141 grism spectrum, the $\text{H}\beta-f_{\text{esc}}$ method is not applicable because of the following reasons. First, estimating the nebular absorption of LyC photons using $\text{H}\beta$ still relies on the assumptions of isotropy and a uniform stellar population (Izotov et al. 2016; Flury et al.

2022). Given the pronounced spatial inhomogeneity of the LyC signal in J1244-LyC1 (4.2), we expect that the galaxy-integrated f_{esc} inferred from $\text{H}\beta$ would significantly deviate from the true value. Second, J1244-LyC1 is substantially more dusty than most LyC candidate samples, and $\text{H}\beta$ only constrains the nebular absorption of LyC photons, providing no information on the additional attenuation by dust (Jaskot 2025). This makes the method particularly unsuitable for J1244-LyC1. Finally, the SNR of $\text{H}\beta$ is relatively low, which prevents us from placing strong constraints on f_{esc} using this approach.

We adopt the third approach to estimate the escape fraction. The relative escape fraction is commonly defined between the rest-frame LyC and UV bands as

$$f_{\text{esc,rel}} = \frac{(L_{\text{LyC}}/L_{\text{UV}})_{\text{int}}}{(F_{\text{LyC}}/F_{\text{UV}})_{\text{obs}}} \times t_{\text{IGM}}^{-1}, \quad (3)$$

where $(L_{\text{LyC}}/L_{\text{UV}})_{\text{int}}$ is the intrinsic LyC-to-UV luminosity ratio (typically evaluated at $\lambda_{\text{LyC}} = 900 \text{ \AA}$ and $\lambda_{\text{UV}} = 1500 \text{ \AA}$), $t_{\text{IGM}} = e^{-\tau_{\text{IGM}}}$ represents the transmis-

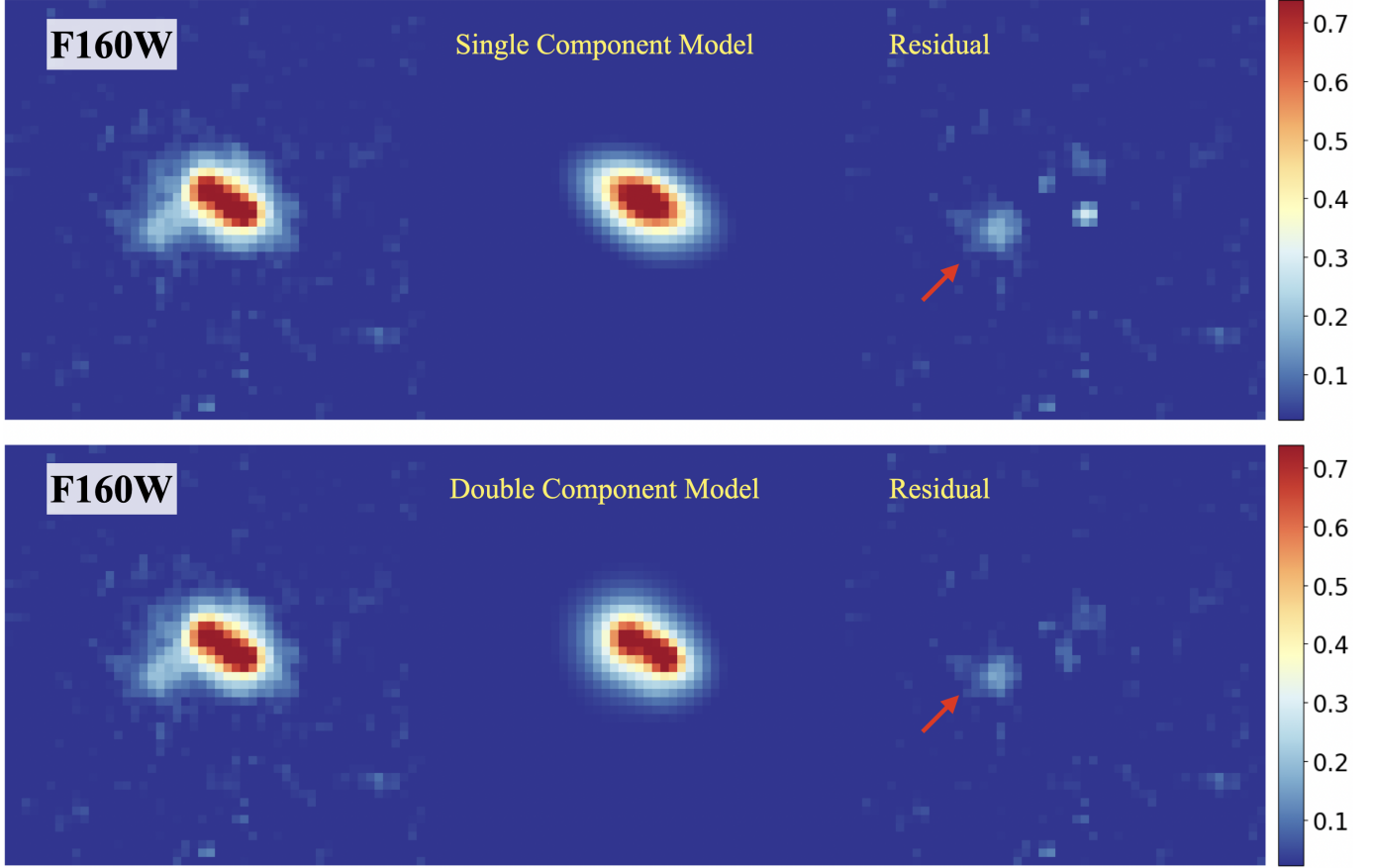


Figure 4. GALFIT decomposition of J1244-LyC1 in HST F160W imaging. All images are normalized to the peak value of the observed image. Single-component (TOP) and Double-component (BOTTOM) GALFIT models for the F160W image. The Double-component fit provides a significantly better description of the main body of J1244-LyC1, whereas the single-component model leaves behind prominent structural residuals. The red arrows in the residual map highlight the tidal-tail structure, a clear signature of galaxy mergers.

sion fraction of ionizing photons through the IGM, and τ_{IGM} is the IGM opacity (e.g., Steidel et al. 2001; Inoue et al. 2014; Meiksin 2006).

For J1244-LyC1, we compute the relative escape fraction using the observed photometry in the HST/WFC3 UVIS F225W and F475W filters. We treat the F225W band (central wavelength $\sim 665 \text{ \AA}$; $F_{\text{F225W}} = 27.81_{-0.10}^{+0.11}$ AB mag) as the LyC band, and the F475W band (central wavelength $\sim 1400 \text{ \AA}$; $F_{\text{F475W}} = 24.27_{-0.01}^{+0.01}$ AB mag) as the non-ionizing UV band. The intrinsic luminosity ratio, $(L_{\text{F225W}}/L_{\text{F475W}})_{\text{int}} = 7.4$, is obtained directly from our best-fit stellar population models.

The filter throughput weighted IGM transmission, $\bar{\tau}_{\text{IGM}}$ is computed using the IGM absorption prescription of Meiksin (2006), which is also adopted by CIGALE. Following the method of Wang et al. (2025), we calculate the transmission coefficient for each wavelength and then perform a transmission-weighted average over the

F225W bandpass:

$$\bar{\tau}_{\text{IGM}} = \frac{\int e^{-\tau_{\text{IGM}} \frac{T_{\text{F225W}}}{\lambda}} d\lambda}{\int \frac{T_{\text{F225W}}}{\lambda} d\lambda} \quad (4)$$

which yields $\bar{\tau}_{\text{IGM}} \approx 0.12$.

After applying the dust correction (as detailed in Section 3.2.3, adopting $E(B - V) = 0.21$), the absolute escape fraction is derived as

$$f_{\text{esc,abs}} = f_{\text{esc,rel}} \times 10^{-0.4 A_{\text{UV}}}. \quad (5)$$

By following the Calzetti dust attenuation law (Calzetti et al. 2000) appropriate for high- z star-forming galaxies, we adopted $A_{\text{UV}} = 10.33 \times E(B - V)$ and calculated $f_{\text{esc,abs}} = 0.36 \pm 0.04$, which is consistent with the SED result (see Table 2).

4. DISCUSSION

In this section, we examine the uncertainties of f_{esc} calculation, analyze the spatially resolved LyC escape to understand the nature of the massive LyC leakers, and discuss the environmental effects on the LyC leakage.

4.1. f_{esc} Calculation

For an individual high-redshift galaxy, the estimation of f_{esc} is inevitably affected by substantial uncertainties introduced by IGM transmission. In practice, we can only approximate this effect using the average IGM transmission predicted by models at the corresponding redshift. However, given the large sightline-to-sightline variations in IGM properties, f_{esc} and t_{IGM} are intrinsically degenerate (Jaskot 2025; Wang et al. 2025). Consequently, f_{esc} is often overestimated, as LyC leakers are more readily detected along relatively transparent sightlines (Bassett et al. 2021). This represents one of the most significant challenges in LyC studies at high redshift: inferred values of f_{esc} always rely on assumed IGM models (Inoue et al. 2014; Meiksin 2006).

On the other hand, we could directly estimate the f_{esc} by determining the intrinsic LyC flux, $L_{\text{LyC,int}}$. In principle, if the SED fit is sufficiently robust, f_{esc} can be computed simply as $f_{\text{LyC,obs}}/L_{\text{LyC,int}}$. However, as defined in Section 3.5, a commonly adopted approach expresses f_{esc} in terms of the UV flux, introducing $f_{\text{UV,obs}}$. Because $f_{\text{UV,obs}}$ serves as a proxy for the SFR, this method helps mitigate systematic uncertainties associated with the model dependence of SED fitting (Siana et al. 2007; Steidel et al. 2018).

This definition requires an estimate of the intrinsic stellar ratio ($L_{\text{UV}}/L_{\text{LyC}})_\text{int}$, which depends on both the stellar population model inferred from the SED and the specific wavelength ranges used for $L_{\text{LyC,int}}$ and $L_{\text{UV,int}}$. These fluxes are typically defined at 900 Å and 1500 Å (Siana et al. 2007; Steidel et al. 2001). Although Simmonds et al. (2024) argued that defining the intrinsic ratio using 900 Å and 1500 Å can systematically overestimate f_{esc} —and suggested instead adopting fluxes at 700 Å and 1100 Å—this alternative is less suitable at high redshift. Owing to strong IGM absorption, LyC photons near the Lyman limit (e.g., 900 Å) remain substantially more detectable than those at shorter wavelengths such as 700 Å (Inoue et al. 2014). Furthermore, the spectral range between the Lyman limit and Ly α is also significantly affected by the IGM; thus, while the traditional definition may overestimate f_{esc} , it does not introduce additional IGM-related uncertainties and is particularly effective for identifying LyC leakers. Since high-redshift LyC searches are predominantly imaging-based, the definition also depends on filter choice, as discussed in Section 3.5.

Although the ratio ($L_{\text{UV}}/L_{\text{LyC}})_\text{int}$ primarily reflects the underlying stellar population, it can, in principle, span a broad range. Empirically, typical values fall between 3 and 7 (e.g., Guaita et al. 2017; Alavi et al. 2020; Rutkowski et al. 2017; Smith et al. 2018; Wang

et al. 2025). We note that the value derived for J1244-LyC1 slightly exceeds this range, largely because the rest-frame wavelength probed by the F225W filter is bluer and therefore intrinsically fainter than $F_{\text{rest},900}$.

4.2. Spatially resolved LyC escape

The LyC emission of J1244-LyC1 is detected at a significance level of 10σ , and its spatial distribution exhibits a clear clumpy morphology (see Fig. 5). This suggests that different LyC-emitting clumps may have distinct formation mechanisms. To quantitatively identify the locations and centroids of these clumps, we employed a growth-curve algorithm. Specifically, we centered circular apertures on different spatial positions and gradually increased the aperture radius to identify independent LyC-emitting regions with $\text{SNR} > 3$ that do not spatially overlap. Through testing, we found that adopting a maximum radius of 2.5 pixels effectively separates the LyC emission into three independent components—clumps A, B, and C—all with $\text{SNR} > 3$.

In principle, f_{esc} can be independently calculated for each of the three LyC-emitting clumps, which requires determining their respective intrinsic flux ratios ($f_{\text{UV,int}}/f_{\text{LyC,int}}$) from SED fitting (Siana et al. 2007; Steidel et al. 2018). However, since only four high-resolution imaging bands are available, it is difficult to obtain reliable SED fits at each position, and therefore the derived f_{esc} values would be highly uncertain. We therefore assume that their stellar populations are consistent with that of the global merger system as inferred from the integrated SED, and that the dust distribution is spatially uniform. Under this assumption, we estimate that the f_{esc} of clump A is around 1, while the f_{esc} values of clumps B and C are significantly above 1.

It is evident that the f_{esc} values of clumps A, B, and C are substantially overestimated. Overall, the most likely cause of this overestimate is the systematic uncertainty introduced by the choice of IGM model. To ensure consistency between the CIGALE SED-fitting results and our f_{esc} calculations, we adopted the same IGM model implemented in CIGALE (Meiksin 2006). However, as shown in Inoue et al. (2014), different IGM models exhibit very large discrepancies. For J1244-LyC1 at $z = 2.387$, the predicted \bar{t}_{IGM} values vary widely: Meiksin (2006) gives ~ 0.12 , Steidel et al. (2018) gives ~ 0.26 , and Inoue et al. (2014) gives ~ 0.33 . As a result, the inferred f_{esc} may differ by a factor of 2–3 depending on the adopted IGM model. This is one of the primary reasons why the f_{esc} values of all three clumps are collectively overestimated.

In addition, the three clumps show strong internal differences in their inferred escape fractions: clumps B and

C exhibit significantly higher f_{esc} than clump A. For clump A, which is spatially coincident with the main stellar body of the galaxy, the assumption of stellar population consistency is most reasonable. Its f_{esc} is significantly higher than the system-wide average, indicating that the global f_{esc} likely represents a luminosity-weighted average of regions with locally higher escape fractions. This scenario is consistent with observations and models in which ionizing photons escape through low- N_{HI} sightlines (i.e., holes or channels), while the non-ionizing UV continuum is dominated by the integrated stellar population along the entire line of sight (Jaskot 2025; Giovinazzo et al. 2025).

For clumps B and C, our calculations yield results with $f_{\text{esc,abs}} > 1$, which are significantly higher than that of clump A. Both regions are spatially offset from the main stellar body and contribute only minor flux fractions in multi-band imaging. Thus, assuming identical stellar populations as the integrated SED fit is likely invalid; their stellar populations are probably much younger. If we instead assume $f_{\text{esc}} = 1$ for these two regions, we can constrain their intrinsic stellar flux ratios ($f_{\text{UV}}/f_{\text{LyC}}$)_{int} to be $\lesssim 3.5$ and $\lesssim 2.5$, respectively. This implies that the star formation histories in these regions are more bursty and short-lived compared to the overall system. Another important factor is the distribution of dust (Ji et al. 2025). During the merging process, dust can rapidly enrich and remain spatially inhomogeneous on short timescales, enhancing anisotropic escape of LyC photons (Ejdetjärn et al. 2025). Both effects directly impact our estimation of local f_{esc} values for individual LyC-emitting clumps.

A complementary piece of evidence comes from the [O II] map. While [O II] emission traces star formation on short (~ 3 –10 Myr) timescales, the UV continuum traces star formation over longer (~ 10 –100 Myr) timescales (Kennicutt & Evans 2012). We measured the fractional contributions of clumps A, B, and C to the total flux—defined as the flux within a central 0.6'' aperture—in both the UV continuum band (F475W) and the [O II] map. The three clumps exhibit substantial differences in their relative flux contributions between the UV continuum band and the [O II] map (see Table 3). Considering if the three clumps share similar dust attenuation and stellar populations, their fractional [O II] fluxes should be consistent with their UV continuum fractions. The discrepancies for clumps B and C, therefore, indicate that $f_{\text{esc}} > 1$ likely arises from either incorrect dust attenuation estimates or a mismatch between their intrinsic stellar populations and the globally fitted model.

Therefore, to determine the spatial distribution of f_{esc} , it is essential not only to identify individual LyC-emitting clumps but also to obtain high spatial resolution SED and dust maps.

It is worth noting that, to date, J1244-LyC1 and Haro 11 (Komarova et al. 2024) are the only systems that exhibit a clearly multi-clump spatial distribution of LyC leakage, and both are merger systems. Haro 11 is an extreme dwarf starburst galaxy hosting dozens of young massive clusters. Its three LyC-emitting knots show pronounced differences in their stellar populations. Although we cannot assert that J1244-LyC1 is a direct high-redshift analogue of Haro 11, the similarities between the two systems are noteworthy. This may suggest the existence of a LyC photon leakage mechanism that does not strongly evolve with redshift.

4.3. Do mergers boost LyC escape?

Galaxy mergers as a mechanism for promoting LyC photon escape have long been actively discussed (Jaskot 2025; Reste et al. 2025b; Zhu et al. 2024; Yuan et al. 2024; Kostyuk & Ciardi 2024). At low redshift, the LaCOS survey constructed a sample of LyC leakers (Reste et al. 2025a), among which approximately 41% exhibit merger signatures (Reste et al. 2025b). During the cosmic noon epoch, mergers also appear to constitute the majority of LyC leakers (Zhu et al. 2024; Yuan et al. 2024), while cosmological simulations suggest that in the EoR, mergers can significantly enhance the reionization process (Kostyuk & Ciardi 2024).

However, how galaxy mergers promote LyC photon escape remains an open question. On one hand, mergers drive the inflow of low-metallicity cold gas into the central regions, possibly triggering central star formation and producing more LyC photons. Stellar feedback could then open low-density escape channels (Puskás et al. 2025; Faria et al. 2025; Garay-Solis et al. 2025; Cenci et al. 2024). On the other hand, mergers strongly disturb the gaseous environment of galaxies, decreasing the covering fraction of neutral gas while making the ISM more turbulent (Garay-Solis et al. 2025; Purkayastha et al. 2022; Puskás et al. 2025). However, as Kostyuk & Ciardi (2024) pointed out, no comprehensive model has yet been established to fully describe this process, as none is currently capable of resolving all relevant scales, including those down to individual molecular clouds. More observational constraints are therefore required to understand whether merger systems promote global LyC escape or whether escape occurs only from specific substructures.

Table 3. Spatially Resolved f_{esc} Calculation of J1244-LyC1

Target	mag _{F225W}	mag _{F475W}	UV fraction ^a	[O II] fraction ^a	(F _{F475W} /F _{F225W}) _{obs}
J1244-LyC1	27.81 ^{+0.11} _{-0.10}	24.27 ^{+0.01} _{-0.01}	1	1	26 ^{+2.9} _{-2.4}
Clump-A	29.14 ^{+0.28} _{-0.23}	26.87 ^{+0.05} _{-0.23}	13.7 ± 0.5%	6.2 ± 2.8%	8.3 ^{+2.6} _{-1.6}
Clump-B	29.27 ^{+0.34} _{-0.27}	27.79 ^{+0.11} _{-0.10}	5.8 ± 0.5%	5.5 ± 2.5%	4.0 ^{+1.5} _{-0.9}
Clump-C	29.44 ^{+0.37} _{-0.28}	28.47 ^{+0.21} _{-0.17}	3.1 ± 0.5%	10.5 ± 2.8%	2.4 ^{+1.1} _{-0.6}

NOTE— All reported uncertainties represent 1σ errors.

^aFraction of the total photometric flux of J1244-LyC1 measured within a $0.6''$ aperture.

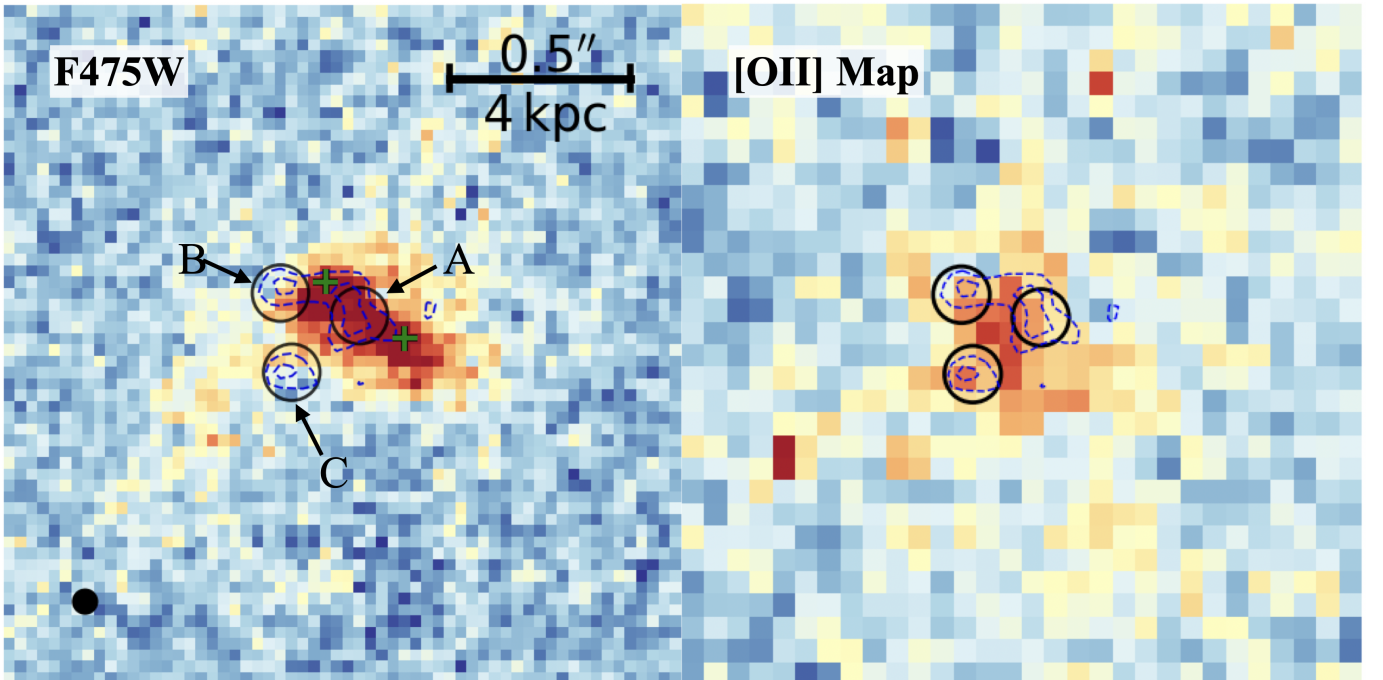


Figure 5. UV morphology and [O II] emission distribution of J1244-LyC1. We present the HST/WFC3 F475W image (rest-frame UV continuum) together with the [O II] emission map extracted from the HST WFC3/G141 slitless spectroscopic data. The blue dashed contours trace the spatial distribution of the LyC emission. The green crosses mark the two luminosity centers identified in the F475W image. Three black circles (diameter $0.15''$) indicate the locations of the three LyC-emitting clumps defined in our analysis. At all three clump positions, the flux distribution in F475W differs significantly from that in the [O II] map, highlighting spatial variations in recent ($\sim 3\text{--}10$ Myr) versus longer-timescale ($\sim 10\text{--}100$ Myr) star-formation activity.

The diffuse LyC-band emission observed in J1244-LyC1 provides a unique opportunity to investigate this issue in the high-redshift Universe. We observe spatial variations of LyC photon leakage across different regions of a merger system at cosmic noon. As discussed in Section 4.2, we identify three LyC-leaking clumps in J1244-LyC1. Clump A lies between the two UV-bright centers, while clumps B and C exhibit spatial offsets from the main merger system.

For clumps B and C, the leakage positions are offset by less than $0.5''$ from the main body, similar to other merger-like LyC leakers (Gupta et al. 2024; Yuan et al.

2024). Given their coincidence with the tidal tails, we attribute their LyC photon leakage to star formation occurring within these tidal features. For clump A, however, its position between the two UV-bright centers makes its formation mechanism more uncertain. It is unclear whether the central leakage region belongs to one of the two merging galaxies, lies between them, or is located on the near side of the system. Regardless of the configuration, the presence of clump A distinguishes J1244-LyC1 from other merger-featured LyC candidates: its LyC emission shows no significant spatial offset from the UV morphology. This confirms that

a merger system can indeed produce strong LyC photon escape.

4.4. The Formation of Massive LyC Leakers

A key question worth discussing is whether the formation pathway of J1244-LyC1 differs substantially from that of other known LyC leakers. To date, confirmed LyC leakers at high redshift are predominantly low-mass systems ($M_* \lesssim 10^{9.7} M_\odot$) with very little dust attenuation ($E(B - V) \lesssim 0.1$; e.g., Fletcher et al. 2019; Yuan et al. 2024; Gupta et al. 2024; Ji et al. 2025; Shapley et al. 2016; Marques-Chaves et al. 2024; Meštrić et al. 2025; Kim et al. 2023; Rivera-Thorsen et al. 2022; Kerutt et al. 2024). Even in the low-redshift Universe, massive LyC-leaking galaxies remain exceedingly rare, with roughly half of the known leakers having stellar masses below $10^9 M_\odot$ (Flury et al. 2022; Reste et al. 2025a,b; Jaskot 2025). In contrast, J1244-LyC1 is both massive and dusty ($M_* = 10^{10.2} M_\odot$; $E(B - V) = 0.21$), suggesting that its LyC escape mechanism may differ from that of the majority of previously studied systems.

A plausible interpretation is that mergers play a more critical role in enabling LyC escape in massive galaxies. As discussed in Reste et al. (2025b), LyC escape in low-mass, compact star-forming galaxies can be driven primarily by stellar feedback, which efficiently perturbs the ISM owing to their shallow gravitational potentials (e.g., Rey et al. 2022; Trebitsch et al. 2017). The interplay between star formation and feedback in dwarf galaxies may lead to episodic star-formation cycles—the so-called “breathing mode” (Cenci et al. 2024; Stinson et al. 2007; Muratov et al. 2015). During each cycle, central star formation triggers feedback that temporarily quenches further star formation; gas then re-accretes, and the cycle repeats. Such behavior naturally creates low-density channels through which LyC photons can escape.

In massive galaxies, however, stellar feedback alone is generally insufficient to substantially alter the ISM structures (Pandya et al. 2021; Somerville & Davé 2015). Thus, merger-driven processes—which can simultaneously induce intense starbursts and violently reshape the ISM—become far more important for enabling LyC escape. This likely contributes to the extreme rarity of massive LyC leakers.

Nevertheless, both observations and theoretical models consistently show that massive LyC-leaking galaxies are highly unusual. This stands in contrast to the conventional approach for estimating the ionizing photon budget during the EoR, which relies on the UV luminosity function and often assumes that more massive galaxies contribute more escaping ionizing photons. There-

fore, J1244-LyC1 provides a valuable window into the physical mechanisms regulating LyC escape in massive galaxies, offering insight that may help refine our understanding of reionization-era processes.

4.5. Environmental Effects

The impact of the environment on LyC leakage remains an open question. On one hand, an overdense environment may enhance star formation at $z > 1$ (Elbaz et al. 2007; Taamoli et al. 2024); on the other hand, it remains unclear whether such environments facilitate the further escape of LyC photons into the IGM, or how this process evolves with redshift.

For searches targeting LyC leakers, the latter question is particularly relevant. It is commonly assumed that in the high-redshift Universe ($z > 6$), overdense regions—such as protocluster environments—promote LyC photon escape into the IGM, and that Ly α emitters can trace the associated ionized structures. However, at $z < 5.5$, some studies suggest that protocluster environments may be more neutral than the field (Kashino et al. 2025; Mawatari et al. 2017; Liang et al. 2021). This could result from the formation of a circumgalactic medium (CGM) or from continued inflow of cold gas along large-scale structure, though no consensus has been reached.

Against this background, the detection of J1244-LyC1 becomes a particularly intriguing case. Although it does not reside within the BOSS1244 protocluster (at $z \sim 2.24$), it is still affected by the IGM environment associated with the foreground protocluster. While we cannot definitively confirm that the line of sight toward J1244-LyC1 corresponds to a lower-than-average IGM density—as this is directly connected to the measured f_{esc} —we can state with confidence that the presence of such large-scale protocluster structures does not entirely prohibit the detection of background LyC leakers.

Furthermore, there are no foreground galaxies within $\sim 3''$ of J1244-LyC1. This suggests that it is not strongly affected by the CGM of foreground systems—one reason it remains detectable.

This serendipitous finding prompts reconsideration of whether systematic searches for LyC leakers should focus exclusively on protocluster fields. The presence of background LyC leakers may, in fact, provide additional information on the IGM along these lines of sight.

5. SUMMARY

This work presents the first results from the MAMMOTH-LyC ultra-deep HST WFC3/UVIS imaging survey (HST-GO-17159; P.I.: X. Wang), targeting the core regions of two massive galaxy protoclusters

at $z \sim 2.2$. We discover a new strong LyC leaker at $z = 2.39$, named J1244-LyC1, where spatially resolved LyC emission is detected using the ultra-deep F225W imaging acquired by MAMMOTH-LyC. The total LyC-band signal is detected at a 10σ level, with an estimated escape fraction of $f_{\text{esc}} \sim 36\%$, and shows no spatial offset relative to the UV-band imaging (F475W). The galaxy is part of the EELG sample in the MAMMOTH-Grism survey (Wang et al. 2022), and has been observed with HST WFC3/G141 grism spectroscopy, covering [O II], H γ , and H β . In addition, two Keck/MOSFIRE K band spectra cover its H α emission line. These observations robustly confirm the spectroscopic redshift of J1244-LyC1. Within a 3'' radius of J1244-LyC1, no foreground galaxies are found, and no unidentified strong emission lines are detected across 1.1–1.7 μm and 2.0–2.3 μm , confirming the absence of any foreground interloper.

High-resolution imaging across multiple bands reveals that J1244-LyC1 exhibits clear merger signatures—two photometric centers separated by a projected distance of 2.5 kpc and tidal-tail features. Thanks to the two Keck/MOSFIRE K band observations, whose slits were placed at slightly different orientations, we measured a projected velocity difference of $\sim 116 \text{ km s}^{-1}$ between the two photometric components. This confirms that J1244-LyC1 is a major merger in its late stage. Since the global LyC emission shows no spatial offset, this represents the first high- z merger system in which LyC photon escape has been directly confirmed.

We performed multi-band photometric SED fitting for J1244-LyC1 and verified the consistency between the derived physical parameters and the observed emission-line constraints. Because J1244-LyC1 exhibits spatially resolved LyC emission, we are, for the first time, able to study the substructures and physical processes responsible for LyC escape in a high- z sample. Both the photometric centers and the tidal tails show evident LyC leakage. We interpret this as the result of vigorous star formation triggered by the merger process

and the strongly disturbed ISM environment, jointly facilitating LyC photon escape. J1244-LyC1 represents an even rarer case of a massive LyC leaker. We further discuss the critical role of the merger process in enabling LyC escape in massive galaxies—unlike low-mass systems, massive galaxies rely more heavily on the strong ISM disturbances induced by mergers to open low-opacity channels for LyC leakage.

The dynamical structure, Ly α line profile, and spatial distribution of Ly α emission in J1244-LyC1 are therefore of great importance. Follow-up observations with HST and ground-based adaptive-optics IFUs, such as Keck/OSIRIS, will be crucial for further understanding. J1244-LyC1 represents a rare and ideal case for studying the impact of mergers on LyC leakage, providing valuable observational constraints on the role of merger systems in the reionization era.

This work is supported by the National Key R&D Program of China No.2025YFF0510603, the National Natural Science Foundation of China (grant 12373009), the CAS Project for Young Scientists in Basic Research Grant No. YSBR-062, the China Manned Space Program with grant no. CMS-CSST-2025-A06, and the Fundamental Research Funds for the Central Universities. XW acknowledges the support by the Xiaomi Young Talents Program, and the work carried out, in part, at the Swinburne University of Technology, sponsored by the ACAMAR visiting fellowship. This work is also supported by NASA through HST grants HST-GO-16276 and HST-GO-17159. This work is partly based on data obtained through Swinburne Keck program 2025A_W335. RLD is supported by the Australian Research Council through the Discovery Early Career Researcher Award (DECRA) Fellowship DE240100136 funded by the Australian Government. We wish to extend special thanks to those of Hawaiian ancestry on whose sacred mountain we are privileged to be guests. Without their generous hospitality, most of the observations presented herein would not have been possible.

REFERENCES

Alavi, A., Colbert, J., Teplitz, H. I., et al. 2020, ApJ, 904, 59, doi: [10.3847/1538-4357/abbd43](https://doi.org/10.3847/1538-4357/abbd43)

Amorín, R. O., Rodríguez-Henríquez, M., Fernández, V., et al. 2024, A&A, 682, L25, doi: [10.1051/0004-6361/202449175](https://doi.org/10.1051/0004-6361/202449175)

Bait, O., Borthakur, S., Schaerer, D., et al. 2024, A&A, 688, A198, doi: [10.1051/0004-6361/202348416](https://doi.org/10.1051/0004-6361/202348416)

Barrow, K. S. S., Robertson, B. E., Ellis, R. S., et al. 2020, ApJL, 902, L39, doi: [10.3847/2041-8213/abbd8e](https://doi.org/10.3847/2041-8213/abbd8e)

Bassett, R., Ryan-Weber, E. V., Cooke, J., et al. 2021, MNRAS, 502, 108, doi: [10.1093/mnras/stab070](https://doi.org/10.1093/mnras/stab070)

Beckett, A., Rafelski, M., Scarlata, C., et al. 2025, The Parallel Ionizing Emissivity Survey (PIE). I. Survey design and selection of candidate Lyman Continuum leakers at 3.1 z 3.5. <https://arxiv.org/abs/2503.20878>

Boquien, M., Burgarella, D., Roehlly, Y., et al. 2019, *A&A*, 622, A103, doi: [10.1051/0004-6361/201834156](https://doi.org/10.1051/0004-6361/201834156)

Bridge, C. R., Teplitz, H. I., Siana, B., et al. 2010, *ApJ*, 720, 465, doi: [10.1088/0004-637X/720/1/465](https://doi.org/10.1088/0004-637X/720/1/465)

Bruzual, G., & Charlot, S. 2003, *MNRAS*, 344, 1000, doi: [10.1046/j.1365-8711.2003.06897.x](https://doi.org/10.1046/j.1365-8711.2003.06897.x)

Cai, Z., Fan, X., Peirani, S., et al. 2016, *ApJ*, 833, 135, doi: [10.3847/1538-4357/833/2/135](https://doi.org/10.3847/1538-4357/833/2/135)

Cai, Z., Fan, X., Yang, Y., et al. 2017, *ApJ*, 837, 71, doi: [10.3847/1538-4357/aa5d14](https://doi.org/10.3847/1538-4357/aa5d14)

Calzetti, D., Armus, L., Bohlin, R. C., et al. 2000, *ApJ*, 533, 682, doi: [10.1086/308692](https://doi.org/10.1086/308692)

Carr, C., Cen, R., McCandliss, S., et al. 2025, Supernovae Driven Winds Impede Lyman Continuum Escape from Dwarf Galaxies in First 10 Myr. <https://arxiv.org/abs/2510.21197>

Carter, D. D., Carleton, T., Henningsen, D., et al. 2025, SKYSURF-10: A Novel Method for Measuring Integrated Galaxy Light. <https://arxiv.org/abs/2507.05323>

Cenci, E., Feldmann, R., Gensior, J., et al. 2024, *MNRAS*, 527, 7871, doi: [10.1093/mnras/stad3709](https://doi.org/10.1093/mnras/stad3709)

Charlot, S., & Fall, S. M. 2000, *ApJ*, 539, 718, doi: [10.1086/309250](https://doi.org/10.1086/309250)

Chisholm, J., Orlitová, I., Schaefer, D., et al. 2017, *A&A*, 605, A67, doi: [10.1051/0004-6361/201730610](https://doi.org/10.1051/0004-6361/201730610)

Chisholm, J., Saldana-Lopez, A., Flury, S., et al. 2022, *MNRAS*, 517, 5104, doi: [10.1093/mnras/stac2874](https://doi.org/10.1093/mnras/stac2874)

Choustikov, N., Katz, H., Saxena, A., et al. 2024, *MNRAS*, 529, 3751, doi: [10.1093/mnras/stae776](https://doi.org/10.1093/mnras/stae776)

Dayal, P., Volonteri, M., Schneider, R., et al. 2020, *MNRAS*, 495, 3065, doi: [10.1093/mnras/staa1138](https://doi.org/10.1093/mnras/staa1138)

Ejdetjärn, T., Agertz, O., Renaud, F., et al. 2025, *Monthly Notices of the Royal Astronomical Society*, 543, 3849–3866, doi: [10.1093/mnras/staf1733](https://doi.org/10.1093/mnras/staf1733)

Elbaz, D., Daddi, E., Le Borgne, D., et al. 2007, *Astronomy & Astrophysics*, 468, 33–48, doi: [10.1051/0004-6361:20077525](https://doi.org/10.1051/0004-6361:20077525)

Faria, L., Patton, D. R., Courteau, S., Ellison, S., & Brown, W. 2025, Interacting galaxies in the IllustrisTNG simulations – VIII: Pericentric star formation rate enhancements are driven both by increased fuelling and efficiency. <https://arxiv.org/abs/2501.14031>

Ferreira, L., Ellison, S. L., Patton, D. R., et al. 2024, Galaxy evolution in the post-merger regime I – Most merger-induced in-situ stellar mass growth happens post-coalescence. <https://arxiv.org/abs/2410.06356>

Finkelstein, S. L., D’Aloisio, A., Paardekooper, J.-P., et al. 2019, Conditions for Reionizing the Universe with A Low Galaxy Ionizing Photon Escape Fraction, doi: [10.3847/1538-4357/ab1ea8](https://doi.org/10.3847/1538-4357/ab1ea8)

Fletcher, T. J., Tang, M., Robertson, B. E., et al. 2019, *The Astrophysical Journal*, 878, 87, doi: [10.3847/1538-4357/ab2045](https://doi.org/10.3847/1538-4357/ab2045)

Flury, S. R., Jaskot, A. E., Ferguson, H. C., et al. 2022, *The Astrophysical Journal*, 930, 126, doi: [10.3847/1538-4357/ac61e4](https://doi.org/10.3847/1538-4357/ac61e4)

Flury, S. R., Jaskot, A. E., Ferguson, H. C., et al. 2022, *ApJS*, 260, 1, doi: [10.3847/1538-4365/ac5331](https://doi.org/10.3847/1538-4365/ac5331)

Flury, S. R., Jaskot, A. E., Saldana-Lopez, A., et al. 2025, *ApJ*, 985, 128, doi: [10.3847/1538-4357/adc305](https://doi.org/10.3847/1538-4357/adc305)

Fruchter, A. S., & Hook, R. N. 2002, *PASP*, 114, 144, doi: [10.1086/338393](https://doi.org/10.1086/338393)

Garay-Solis, Y., Barrera-Ballesteros, J. K., Carigi, L., et al. 2025, The EDGE-CALIFA Survey: Influence of Mergers on Radial Profiles of Star-Formation Properties. <https://arxiv.org/abs/2509.21852>

Gazagnes, S., Chisholm, J., Schaefer, D., et al. 2018, *A&A*, 616, A29, doi: [10.1051/0004-6361/201832759](https://doi.org/10.1051/0004-6361/201832759)

Giovinazzo, E., Oesch, P. A., Weibel, A., et al. 2025, Breaking Through the Cosmic Fog: JWST/NIRSpec Constraints on Ionizing Photon Escape in Reionization-Era Galaxies. <https://arxiv.org/abs/2507.01096>

Golden-Marx, E., Cai, Z., Shi, D., et al. 2025, Probing the influence of the protocluster environment on galaxy morphology at $z = 2.23$. <https://arxiv.org/abs/2511.14843>

Guaita, L., Talia, M., Pentericci, L., et al. 2017, *A&A*, 606, A19, doi: [10.1051/0004-6361/201730603](https://doi.org/10.1051/0004-6361/201730603)

Gupta, A., Trott, C. M., Jaiswar, R., et al. 2024, MOSEL survey: Spatially offset Lyman-continuum emission in a new emitter at $z=3.088$, arXiv, doi: [10.48550/arXiv.2403.13285](https://doi.org/10.48550/arXiv.2403.13285)

Inoue, A. K., Shimizu, I., Iwata, I., & Tanaka, M. 2014, *Monthly Notices of the Royal Astronomical Society*, 442, 1805, doi: [10.1093/mnras/stu936](https://doi.org/10.1093/mnras/stu936)

Izotov, Y. I., Orlitová, I., Schaefer, D., et al. 2016, *Nature*, 529, 178, doi: [10.1038/nature16456](https://doi.org/10.1038/nature16456)

Izotov, Y. I., Orlitová, I., Schaefer, D., et al. 2016a, *Nature*, 529, 178–180, doi: [10.1038/nature16456](https://doi.org/10.1038/nature16456)

Izotov, Y. I., Schaefer, D., Thuan, T. X., et al. 2016b, Detection of high Lyman continuum leakage from four low-redshift compact star-forming galaxies, doi: [10.1093/mnras/stw1205](https://doi.org/10.1093/mnras/stw1205)

Jaskot, A. E. 2025, *Annual Review of Astronomy and Astrophysics*, 63, 45, doi: <https://doi.org/10.1146/annurev-astro-111324-074935>

Jaskot, A. E., Oey, M. S., Scarlata, C., & Dowd, T. 2017, *ApJL*, 851, L9, doi: [10.3847/2041-8213/aa9d83](https://doi.org/10.3847/2041-8213/aa9d83)

Ji, Z., Alberts, S., Zhu, Y., et al. 2025, ApJL, 988, L69, doi: [10.3847/2041-8213/adf194](https://doi.org/10.3847/2041-8213/adf194)

Kashino, D., Lilly, S. J., Matthee, J., et al. 2025, arXiv e-prints, arXiv:2506.03121, doi: [10.48550/arXiv.2506.03121](https://doi.org/10.48550/arXiv.2506.03121)

Kennicutt, R. C., & Evans, N. J. 2012, ARA&A, 50, 531, doi: [10.1146/annurev-astro-081811-125610](https://doi.org/10.1146/annurev-astro-081811-125610)

Kennicutt, Jr., R. C. 1998, ARA&A, 36, 189, doi: [10.1146/annurev.astro.36.1.189](https://doi.org/10.1146/annurev.astro.36.1.189)

Kerutt, J., Oesch, P. A., Wisotzki, L., et al. 2024, A&A, 684, A42, doi: [10.1051/0004-6361/202346656](https://doi.org/10.1051/0004-6361/202346656)

Kewley, L. J., Geller, M. J., & Jansen, R. A. 2004, AJ, 127, 2002, doi: [10.1086/382723](https://doi.org/10.1086/382723)

Kim, K. J., Bayliss, M. B., Rigby, J. R., et al. 2023, Small Region, Big Impact: Highly Anisotropic Lyman-continuum Escape from a Compact Starburst Region with Extreme Physical Properties. <https://arxiv.org/abs/2305.13405>

Komarova, L., Oey, M. S., Krumholz, M. R., et al. 2021, ApJL, 920, L46, doi: [10.3847/2041-8213/ac2c09](https://doi.org/10.3847/2041-8213/ac2c09)

Komarova, L., Oey, M. S., Hernandez, S., et al. 2024, ApJ, 967, 117, doi: [10.3847/1538-4357/ad3962](https://doi.org/10.3847/1538-4357/ad3962)

Kostyuk, I., & Ciardi, B. 2024, Influence of mergers on LyC escape of high redshift galaxies, arXiv, doi: [10.48550/arXiv.2412.04348](https://doi.org/10.48550/arXiv.2412.04348)

Li, Z., Wang, X., Cai, Z., et al. 2022, ApJL, 929, L8, doi: [10.3847/2041-8213/ac626f](https://doi.org/10.3847/2041-8213/ac626f)

Liang, Y., Kashikawa, N., Cai, Z., et al. 2021, ApJ, 907, 3, doi: [10.3847/1538-4357/abcdn93](https://doi.org/10.3847/1538-4357/abcdn93)

Liu, S., Zheng, X. Z., Shi, D. D., et al. 2023, MNRAS, 523, 2422, doi: [10.1093/mnras/stad1543](https://doi.org/10.1093/mnras/stad1543)

Ma, X., Quataert, E., Wetzel, A., et al. 2020, MNRAS, 498, 2001, doi: [10.1093/mnras/staa2404](https://doi.org/10.1093/mnras/staa2404)

Marques-Chaves, R., Schaefer, D., Vanzella, E., et al. 2024, Witnessing an extreme, highly efficient galaxy formation mode with resolved Ly α and LyC emission, doi: [10.1051/0004-6361/202451667](https://doi.org/10.1051/0004-6361/202451667)

Mawatari, K., Inoue, A. K., Yamada, T., et al. 2017, MNRAS, 467, 3951, doi: [10.1093/mnras/stx038](https://doi.org/10.1093/mnras/stx038)

Meiksin, A. 2006, MNRAS, 365, 807, doi: [10.1111/j.1365-2966.2005.09756.x](https://doi.org/10.1111/j.1365-2966.2005.09756.x)

Meštrić, U., Vanzella, E., Beckett, A., et al. 2025, A&A, 698, A203, doi: [10.1051/0004-6361/202451959](https://doi.org/10.1051/0004-6361/202451959)

Muratov, A. L., Kereš, D., Faucher-Giguère, C.-A., et al. 2015, Monthly Notices of the Royal Astronomical Society, 454, 2691–2713, doi: [10.1093/mnras/stv2126](https://doi.org/10.1093/mnras/stv2126)

Naidu, R. P., Tacchella, S., Mason, C. A., et al. 2020, The Astrophysical Journal, 892, 109, doi: [10.3847/1538-4357/ab7cc9](https://doi.org/10.3847/1538-4357/ab7cc9)

Naidu, R. P., Matthee, J., Oesch, P. A., et al. 2022, Monthly Notices of the Royal Astronomical Society, 510, 4582, doi: [10.1093/mnras/stab3601](https://doi.org/10.1093/mnras/stab3601)

Oesch, P. A., Montes, M., Reddy, N., et al. 2018, The Astrophysical Journal Supplement Series, 237, 12, doi: [10.3847/1538-4365/aacb30](https://doi.org/10.3847/1538-4365/aacb30)

Osterbrock, D. E., & Ferland, G. J. 2006, Astrophysics of gaseous nebulae and active galactic nuclei

Pandya, V., Fielding, D. B., Anglés-Alcázar, D., et al. 2021, Monthly Notices of the Royal Astronomical Society, 508, 2979–3008, doi: [10.1093/mnras/stab2714](https://doi.org/10.1093/mnras/stab2714)

Patton, D. R., Torrey, P., Ellison, S. L., Mendel, J. T., & Scudder, J. M. 2013, MNRAS, 433, L59, doi: [10.1093/mnrasl/slt058](https://doi.org/10.1093/mnrasl/slt058)

Pearson, S., Besla, G., Putman, M. E., et al. 2016, MNRAS, 459, 1827, doi: [10.1093/mnras/stw757](https://doi.org/10.1093/mnras/stw757)

Pellegrini, E. W., Oey, M. S., Winkler, P. F., et al. 2012, The Astrophysical Journal, 755, 40, doi: [10.1088/0004-637x/755/1/40](https://doi.org/10.1088/0004-637x/755/1/40)

Prochaska, J. X., Hennawi, J., Cooke, R., et al. 2020, pypeit/PypeIt: Release 1.0.0, v1.0.0, Zenodo, doi: [10.5281/zenodo.3743493](https://doi.org/10.5281/zenodo.3743493)

Purkayastha, S., Kanekar, N., Chengalur, J. N., et al. 2022, ApJL, 933, L11, doi: [10.3847/2041-8213/ac7522](https://doi.org/10.3847/2041-8213/ac7522)

Puskás, D., Tacchella, S., Simmonds, C., et al. 2025, Mergers lighting the early Universe: enhanced star formation, AGN triggering, and Ly α emission in close pairs at $z = 3 - 9$. <https://arxiv.org/abs/2510.14743>

Reste, A., Cannon, J. M., Hayes, M. J., et al. 2023, Tidally offset neutral gas in Lyman continuum emitting galaxy Haro 11. <https://arxiv.org/abs/2301.02676>

Reste, A., Scarlata, C., Hayes, M. J., et al. 2025a, The Astrophysical Journal Supplement Series, 280, 27, doi: [10.3847/1538-4365/adf227](https://doi.org/10.3847/1538-4365/adf227)

Reste, A., Jaskot, A. E., Brazie, J., et al. 2025b, The Ly α and Continuum Origins Survey. III. Investigating the link between galaxy morphology, merger properties and LyC escape. <https://arxiv.org/abs/2509.06922>

Rey, M. P., Pontzen, A., Agertz, O., et al. 2022, MNRAS, 511, 5672, doi: [10.1093/mnras/stac502](https://doi.org/10.1093/mnras/stac502)

Rivera-Thorsen, T. E., Hayes, M., & Melinder, J. 2022, Astronomy & Astrophysics, 666, A145, doi: [10.1051/0004-6361/202243678](https://doi.org/10.1051/0004-6361/202243678)

Rutkowski, M. J., Scarlata, C., Henry, A., et al. 2017, ApJL, 841, L27, doi: [10.3847/2041-8213/aa733b](https://doi.org/10.3847/2041-8213/aa733b)

Sanders, R. L., Shapley, A. E., Topping, M. W., et al. 2025, The AURORA Survey: High-Redshift Empirical Metallicity Calibrations from Electron Temperature Measurements at $z=2-10$. <https://arxiv.org/abs/2508.10099>

Shapley, A. E., Steidel, C. C., Strom, A. L., et al. 2016, ApJL, 826, L24, doi: [10.3847/2041-8205/826/2/L24](https://doi.org/10.3847/2041-8205/826/2/L24)

Shi, D. D., Cai, Z., Fan, X., et al. 2021, ApJ, 915, 32, doi: [10.3847/1538-4357/abfec0](https://doi.org/10.3847/1538-4357/abfec0)

Siana, B., Teplitz, H. I., Colbert, J., et al. 2007, ApJ, 668, 62, doi: [10.1086/521185](https://doi.org/10.1086/521185)

Simmonds, C., Verhamme, A., Inoue, A. K., et al. 2024, MNRAS, 530, 2133, doi: [10.1093/mnras/stae1003](https://doi.org/10.1093/mnras/stae1003)

Smith, B. M., Windhorst, R. A., Jansen, R. A., et al. 2018, ApJ, 853, 191, doi: [10.3847/1538-4357/aaa3dc](https://doi.org/10.3847/1538-4357/aaa3dc)

Somerville, R. S., & Davé, R. 2015, ARA&A, 53, 51, doi: [10.1146/annurev-astro-082812-140951](https://doi.org/10.1146/annurev-astro-082812-140951)

Speagle, J. S., Steinhardt, C. L., Capak, P. L., & Silverman, J. D. 2014, ApJS, 214, 15, doi: [10.1088/0067-0049/214/2/15](https://doi.org/10.1088/0067-0049/214/2/15)

Stark, D. P. 2016, Annual Review of Astronomy and Astrophysics, 54, 761, doi: [10.1146/annurev-astro-081915-023417](https://doi.org/10.1146/annurev-astro-081915-023417)

Steidel, C. C., Bogosavljevic, M., Shapley, A. E., et al. 2018, The Astrophysical Journal, 869, 123, doi: [10.3847/1538-4357/aaed28](https://doi.org/10.3847/1538-4357/aaed28)

Steidel, C. C., Pettini, M., & Adelberger, K. L. 2001, ApJ, 546, 665, doi: [10.1086/318323](https://doi.org/10.1086/318323)

Stierwalt, S., Besla, G., Patton, D., et al. 2015, ApJ, 805, 2, doi: [10.1088/0004-637X/805/1/2](https://doi.org/10.1088/0004-637X/805/1/2)

Stinson, G. S., Dalcanton, J. J., Quinn, T., Kaufmann, T., & Wadsley, J. 2007, ApJ, 667, 170, doi: [10.1086/520504](https://doi.org/10.1086/520504)

Taamoli, S., Mobasher, B., Chartab, N., et al. 2024, The Astrophysical Journal, 966, 18, doi: [10.3847/1538-4357/ad32c5](https://doi.org/10.3847/1538-4357/ad32c5)

Tang, M., Stark, D. P., Chevallard, J., & Charlot, S. 2019, MNRAS, 489, 2572, doi: [10.1093/mnras/stz2236](https://doi.org/10.1093/mnras/stz2236)

Trebitsch, M., Blaizot, J., Rosdahl, J., Devriendt, J., & Slyz, A. 2017, Monthly Notices of the Royal Astronomical Society, 470, 224–239, doi: [10.1093/mnras/stx1060](https://doi.org/10.1093/mnras/stx1060)

Vanzella, E., Nonino, M., Cupani, G., et al. 2018, Monthly Notices of the Royal Astronomical Society: Letters, 476, L15–L19, doi: [10.1093/mnrasl/sly023](https://doi.org/10.1093/mnrasl/sly023)

Wang, B., Heckman, T. M., Amorín, R., et al. 2021, ApJ, 916, 3, doi: [10.3847/1538-4357/ac0434](https://doi.org/10.3847/1538-4357/ac0434)

Wang, X., Li, Z., Cai, Z., et al. 2022, ApJ, 926, 70, doi: [10.3847/1538-4357/ac3974](https://doi.org/10.3847/1538-4357/ac3974)

Wang, X., Teplitz, H. I., Smith, B. M., et al. 2025, The Astrophysical Journal, 980, 74, doi: [10.3847/1538-4357/ada4ab](https://doi.org/10.3847/1538-4357/ada4ab)

Yang, Y., Wang, X., He, X., et al. 2025, MAMMOTH-Grism: Revisiting the Mass-Metallicity Relation in Protocluster Environments at Cosmic Noon. <https://arxiv.org/abs/2511.16154>

Yuan, F.-T., Zheng, Z.-Y., Jiang, C., et al. 2024, Merging Signatures in an Offset Lyman Continuum Emitter at Redshift 3.8, arXiv, doi: [10.48550/arXiv.2409.20352](https://doi.org/10.48550/arXiv.2409.20352)

Zhou, H., Wang, X., Malkan, M. A., et al. 2025, arXiv e-prints, arXiv:2505.04212, doi: [10.48550/arXiv.2505.04212](https://doi.org/10.48550/arXiv.2505.04212)

Zhu, S., Zheng, Z.-y., Yuan, F.-T., Jiang, C., & Lin, R. 2024, Lyman Continuum Leakers at $z > 3$ in the GOODS-S Field: Mergers Dominated, arXiv, doi: [10.48550/arXiv.2412.08395](https://doi.org/10.48550/arXiv.2412.08395)

APPENDIX

A. ASTRODRIZZLE INPUT PARAMETERS

Our input parameters for `Astrodrizzle` are listed in Table 4.

Table 4. AstroDrizzle Parameters

Parameter	Value	Description
<code>skysub</code>	True	Perform sky subtraction
<code>skymethod</code>	globalmin+match	Sky estimation method
<code>driz_sep_scale</code>	0.03	Pixel scale for separate drizzle (arcsec/pixel)
<code>combine_type</code>	imedian	Final combine method
<code>combine_nsigma</code>	4 3	Low/high sigma clipping thresholds
<code>combine_grow</code>	1	Pixel grow radius for rejection
<code>driz_cr</code>	True	Cosmic-ray rejection enabled
<code>driz_cr_corr</code>	True	Cosmic-ray correction enabled
<code>final_wht_type</code>	IVM	Inverse-variance weighting
<code>final_kernel</code>	square	Drizzle kernel
<code>final_pixfrac</code>	0.8	Pixel fraction for final drizzle

B. KECK DATA REDUCTION

The reduction of Keck MOSFIRE data was performed using the PypeIt pipeline (Prochaska et al. 2020). The standard processing sequence included flat-fielding, dark subtraction, cosmic ray detection and slit tracing. Wavelength calibration was derived directly from OH sky lines present in the science frames. One-dimensional spectra were subsequently generated using the Optimal Extraction algorithm. Regarding object identification, the pipeline is configured by default to extract objects in the slit center. While this setup was successful for most sources in Zhou et al. (2025), J1244-LyC1 in the first observations was offset from the slit center, causing the default automatic tracing algorithm to fail. Consequently, we lowered the required signal-to-noise ratio threshold to successfully trace and extract this specific source. Flux calibration was achieved using standard star observations processed identically to the science targets. A specific modification was required for the second set of observations, which utilized the long-slit mode. The default PypeIt configuration treats long-slit data as star traces; this misinterpretation leads to failures in source extraction. To resolve this, we customized the slit parameters by manually adding the slit traces to force extraction, which enabled PypeIt to correctly identify and extract the source.

C. SPECTRUM

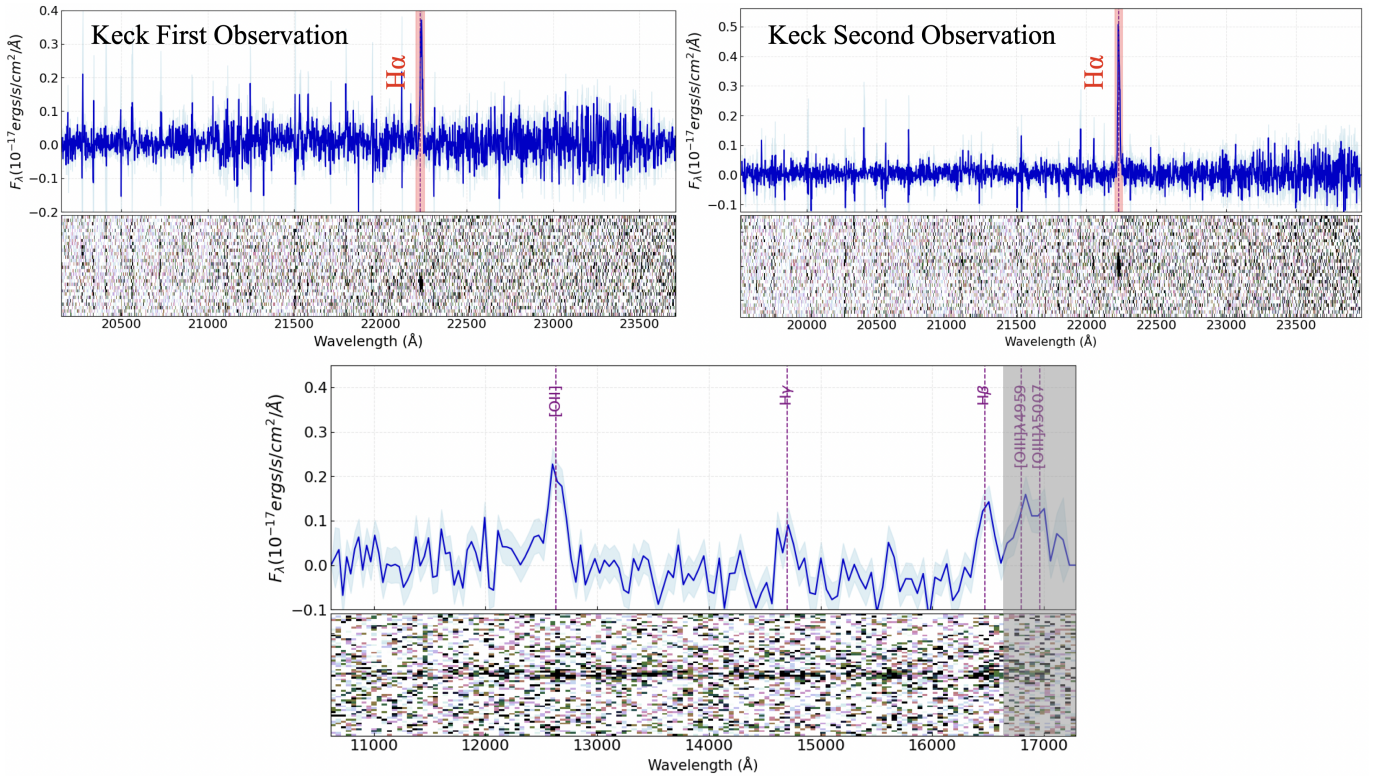


Figure 6. Spectroscopic observations of J1244-LyC1. TOP LEFT and TOP RIGHT PANELS: Keck MOSFIRE K band spectra. BOTTOM PANEL: HST WFC3/G141 grism spectrum, with the region affected by the G141 edge indicated by the gray shaded area.